

Rectification of ENSO Variability by Interdecadal Changes in the Equatorial Background Mean State in a CGCM Simulation

BORIS DEWITTE

Laboratoire d'Etude en Géophysique et Océanographie Spatiale, Toulouse, France

SANG-WOOK YEH

Korea Ocean Research and Development Institute, Ansan, South Korea

BYUNG-KWON MOON

Division of Science Education/Institute of Science Education, Chonbuk National University, Jeonju, South Korea

CAROLE CIBOT AND LAURENT TERRAY

CERFACS URA 1875, Toulouse, France

(Manuscript received 6 December 2005, in final form 7 September 2006)

ABSTRACT

The link between the changes in equatorial background stratification and El Niño–Southern Oscillation (ENSO) modulation is investigated using a simulation from a 260-yr-long coupled general circulation model (CGCM). The work focuses on the role of nonlinearities associated with equatorial wave dynamics. As a first step, the low-frequency change in mean stratification is diagnosed and documented from the shallow-water parameters derived from a vertical mode decomposition of the CGCM. The parameters vary differently according to the baroclinic mode order, which may explain why a flattening thermocline does not necessarily lead to reduced ENSO activity. Estimations of baroclinic mode contributions to zonal current anomalies indicate that the decadal variability projects differently for the baroclinic modes as compared to the interannual variability. In particular, the high-order modes associated with decadal variability have a more pronounced signature in the western Pacific, whereas that associated with interannual variability (i.e., ENSO) shows more energy in the eastern Pacific.

In the light of the results of the CGCM vertical mode decomposition, an intermediate coupled model (ICM) is used to test whether the nonlinearities associated with the changes in the baroclinic mode energy distribution can lead to coherent ENSO modulation. The results indicate that rectification of the interannual variability (ENSO time scales) by the interdecadal variability associated with changes in the oceanic mean states takes place in the ICM. The rectified effect results mostly in an increased variability and skewness of the zonal advection, which tends to produce a zonal seesaw of the sea surface temperature anomaly. A tropical mechanism for producing ENSO modulation is then proposed that reconciles both the rectified effect resulting from nonlinearities associated with equatorial wave dynamics and the tropical decadal mode of thermocline depth arising from Ekman-pumping anomalies located in the central South Pacific.

1. Introduction

During the past 15 yr, the evolution of El Niño events has changed substantially (Trenberth 1997). The most recent striking evidence of these changes is the climate

shift in the Pacific circulation centered in the Tropics that occurred in the late 1970s (Miller et al. 1994a; Trenberth and Hurrell 1994; Zhang et al. 1997; Guilderson and Schrag 1998; Urban et al. 2000). In particular, before about 1976/77, El Niño events tended to develop first along the coast of South America and then spread westward, as was found in the composites of Rasmusson and Carpenter (1982) based on six warm ENSO events from 1951 to 1972. More recent events

Corresponding author address: Boris Dewitte, 14 av. Edouard Belin, 31400 Toulouse, France.
E-mail: boris.dewitte@cnes.fr

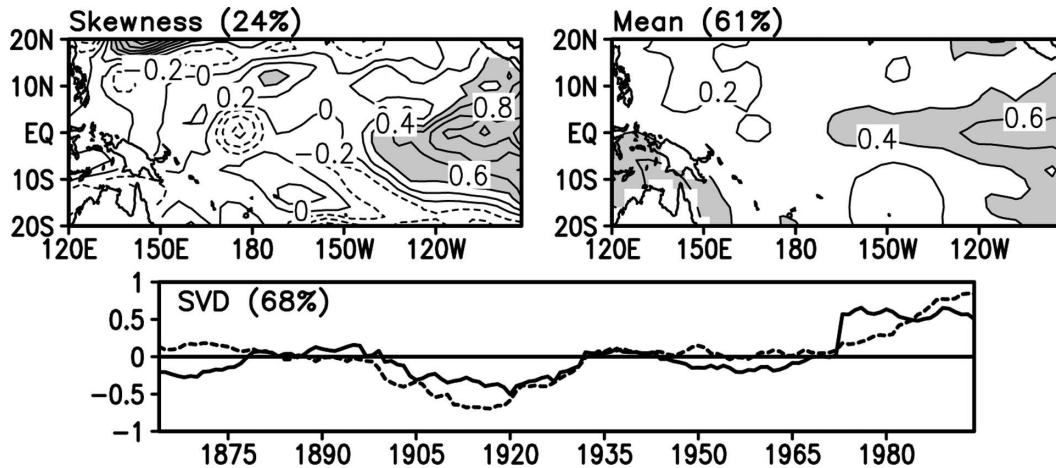


FIG. 1. Distributions of the first SVD mode associated with (left) 21-yr moving skewness of SST anomalies (trend was removed in each window) and (right) 21-yr moving-averaged SST anomalies. The data are the monthly mean global SST data from the National Climatic Data Center (Smith and Reynolds 2004), covering the period from 1854 to the present. Solid and dotted lines indicate the PC time series associated with 21-yr moving skewness of SST anomalies and the 21-yr moving-averaged SST anomalies, respectively. The fractions of covariance/variance of normalized data fields explained by this mode are indicated in titles. Values larger than 0.4 are shaded. (bottom) The correlation between two PC time series is 0.77 (after An 2004).

developed first in the central Pacific and then spread eastward (e.g., Wang 1995). Superimposed on these abrupt climate changes, decadal to interdecadal modes were also observed in the Pacific (Miller et al. 1994b; Trenberth and Hurrell 1994; Tourre et al. 1999). The most clearly identified of these modes, and the one that has been studied the most, is usually referred to as the Pacific Decadal Oscillation (PDO; Mantua and Hare 2002).

Thus far, it has not been clear whether each of these components of the decadal to interdecadal variability in the Pacific is the cause or the effect of the low-frequency modulation of ENSO as observed in the tropical Pacific (Gu and Philander 1995; Torrence and Webster 1999). In fact, there is an ongoing debate in the climate literature as to whether the tropical Pacific decadal variability (TPDV) is generated by coupled processes within the Tropics (Knutson et al. 1997; Kirtman and Schopf 1998; Vimont et al. 2002; Timmermann and Jin 2002; Timmermann et al. 2003; Timmermann 2003), or whether it involves interactions with the extratropics (Latif and Barnett 1994, 1996; Barnett et al. 1999; Gu and Philander 1997; McCreary and Lu 1994; Kleeman et al. 1999).

Within these two broad categories there are a number of competing hypotheses. Among those who argue for a tropically generated TPDV, there is also a controversy over whether TPDV should be understood as being stochastically excited or as being the result of nonlinearities in the coupled tropical system. Regarding the latter scenario, recent modeling studies have

investigated the El Niño–La Niña asymmetry, which has provided a simple way of measuring the nonlinearity of ENSO in the tropical Pacific (Rodgers et al. 2004; Cibot et al. 2005, hereafter CMTD05). They found that the ENSO nonlinearity (as measured by pattern asymmetries) can account for the dominant structure of TPDV in their model. Similarly, the nonlinearity of ENSO diagnosed through nonlinear dynamical heating (NDH) can explain the huge bursts of ENSO activity observed in the 1982/83 and 1997/98 El Niños (An and Jin 2004). Diagnosing ENSO nonlinearity from skewness of sea surface temperature anomalies (SSTAs) in the tropical Pacific, An (2004) further showed that interdecadal change in the latter is associated with interdecadal SST variations in the tropical eastern Pacific (Fig. 1). In particular, the interaction between the ENSO nonlinearity and interdecadal SST variations, as shown in the principal component (PC) time series of Fig. 1, was especially dominant during 1895–1935 and 1975–2003. All of these results suggest the existence of nonlinear positive feedback between ENSO low-frequency modulation and ENSO nonlinearity.

Among all of the sources of nonlinearities in the tropical Pacific system, of particular interest is the one associated with changes in the mean equatorial thermocline. Previous coupled modeling studies on decadal ENSO modulations have shown that the ENSO frequency and amplitude are very sensitive to changes in the position of the equatorial thermocline. Most of them showed that increased ENSO variability tends to be associated with periods in which the thermocline is

deeper in the eastern equatorial Pacific, while weaker ENSO variability tends to be associated with a shallower thermocline (Kirtman and Schopf 1998; Kleeman et al. 1999; Barnett et al. 1999; Timmermann et al. 1999; Timmermann 2001; Rodgers et al. 2004; CMTD05). It has been pointed out that this relationship between thermocline tilt and ENSO activity is counterintuitive in a linear model sense (i.e., for which the background state is fixed), because it is in that configuration that a small vertical displacement of the thermocline would have a maximum impact on the temperature of water, which upwells into the surface mixed layer in the Niño-3 region (5°N – 5°S , 90° – 150°W). However, this argument ignores the fact that changes in the thermocline tilt are associated with a redistribution of energy for baroclinic modes, which has the potential of affecting ENSO properties at decadal time scales (Dewitte 2000, hereafter DEW; Yeh et al. 2001). Also, considering the difference in mean vertical stratification between the western and eastern equatorial Pacific, decadal changes in thermocline tilt may be associated with a different dynamic response of the ocean to the advection terms affecting the SST. These peculiarities need to be considered with regards to nonlinearities that can be produced within the tropical Pacific system and associated changes of ENSO activity. In this context, the issues of whether the ENSO modulation leads or is ahead of the changes in mean state needs to be addressed. For instance, CMTD05 found that the ENSO modulation tends to lead (by ~ 1 yr) the change in subsurface temperature (their Fig. 17), which is also somehow counterintuitive. An investigation of the impact of changes in mean equatorial stratification on the SST tendency terms associated with equatorial wave dynamics may provide material for interpreting such characteristics.

As a first step toward validation of the equatorially based models for explaining observed interdecadal variations, it therefore appears necessary to estimate the characteristics of the oceanic patterns that can lead to the changes in the equatorial wave dynamics, and consecutively to changes in the coupled instabilities. This is the preliminary objective of this study. The “data” used are the output from the state-of-the-art coupled model. Considering the complete physics of the model and the time span of the simulation (260 yr), it enables access to realistic variations in parameters at decadal time scales, which remain difficult to obtain from temporally and spatially limited observations. In addition, simulation with a full-physics, global coupled model ensures that most of the coupled processes are taken into account. The Simple Ocean Data Assimilation (SODA) dataset (Carton et al. 2000), which spans 50 yr, was also used each time it could help check the

consistency of our findings. The simulation used for this study has already been investigated in previous recent works (CMTD05; Tourre et al. 2005). These studies documented the decadal to interdecadal variability in the simulation and showed that it is realistic in many aspects. In particular, despite an ENSO mode with a dominant quasi-biennial frequency, the decadal to interdecadal variability for SST, thermocline depth, and sea level pressure as revealed from EOF and singular value decomposition (SVD) analyses share many characteristics with the observations, and the ENSO modulation in the model has a realistic amplitude and time scale. To check for the relationship between ENSO nonlinearity and the change in mean state of the model, calculations similar to those of An (2004) were performed. The results are shown in Fig. 2 and can be compared directly with those in Fig. 1. Interestingly, the model also reveals a strong relationship between ENSO nonlinearity (as measured by the skewness of SSTAs) and the mean state, with the latter apparently being ahead by ~ 10 yr for some periods. The model’s spatial patterns also resemble those of the observations, which enable a more thorough analysis.

The specific scientific questions dealt with in this paper are therefore as follows: What is the signature of the decadal variability in the equatorial vertical mode characteristics? Does the vertical structure variability contribute to the ENSO modulation through changes in the equatorial wave dynamics and associated nonlinearities? Furthermore, do the changes in mean states lead or lag behind the ENSO modulation?

To support our investigation we used an intermediate coupled model (ICM) of the tropical Pacific to test ideas and study the impact of changes in the background mean state and model parameters as derived from the coupled general circulation model (CGCM) simulation on the simulated ENSO variability.

The paper is organized as follows. Section 2 is devoted to the coupled models and data descriptions. Section 3 documents the vertical structure’s decadal variability simulated by the CGCM and associated equatorial wave parameters. Section 4 explores the sensitivity of the ICM to decadal forcing of the equatorial wave parameters. In the light of the results, a mechanism for decadal variability in the tropical Pacific is proposed in section 5, followed by concluding remarks.

2. Coupled models and data descriptions

a. ARPEGE-OPA (hereafter ARPA)

The ocean component ORCA2 used was the global configuration of the Océan Parallélisé (OPA) 8 ocean general circulation model (OGCM), a hydrostatic

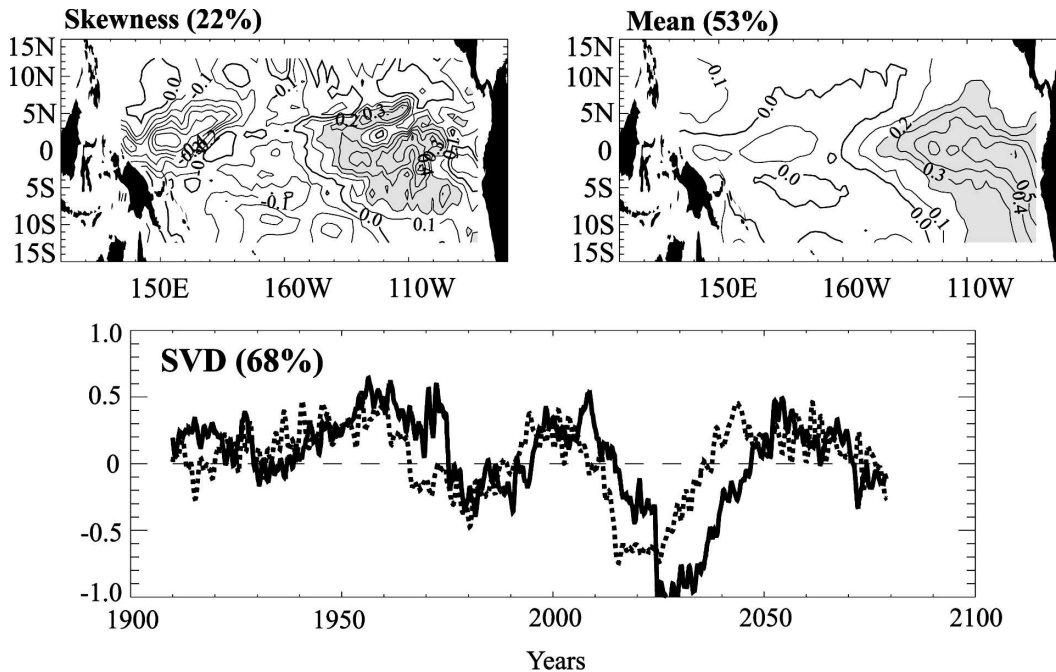


FIG. 2. Same as Fig. 1, but for the CGCM simulation (ARPA).

primitive equation model with a free-surface formulation (Roulet and Madec 2000). The model includes a sea ice component, the Hibler-type dynamic–thermodynamic Louvain-La-Neuve sea ice model (LIM), developed at the Université Catholique de Louvain (UCL) by Fichefet and Morales Maqueda (1997). The atmospheric component used was the third version of the Action de Recherche Petite Echelle Grande Echelle (ARPEGE)-Climat atmospheric general circulation model (AGCM) developed at Météo-France (Déqué et al. 1994). The standard configuration of the climate version employs a T63 triangular horizontal truncation.

The ARPEGE and ORCA/LIM models were coupled through the OASIS 2.5 coupler developed at Centre Européen de Recherche et de Formation Avancée en Calcul Scientifique (CERFACS) (Terray et al. 1995), which ensures the time synchronization between the GCMs and does the spatial interpolation from one grid to another.

The atmospheric initial state was an uncoupled integration of ARPEGE for January. The initial ocean state was taken from Levitus et al. (1998) for temperature and salinity, and was zero for the velocity field. The initial sea ice state was also from Levitus et al. (1998).

From this initial state, the coupled model was integrated for 1 yr. During the first year, an excess of freshwater release occurred in the Labrador Sea, altering the

deep convection of water masses in this region. To correct this bias, the second year of the integration started with Levitus et al. (1998) conditions for temperature and salinity fields. Hence the excess of freshwater was removed from the ocean, enhancing deep convection and limiting sea ice formation in the Arctic region at a more reasonable value. From this point, the integration was pursued over 69 yr to allow the system to reach a quasi-equilibrium state in the upper layers of the ocean. We then integrated the coupled model for 200 yr. We only considered the latest 200-yr period for the subsequent analyses.

More detail on the model configuration and variability can be found in CMTD05.

b. LODCA

LODCA is a tropical Pacific ocean–atmosphere model of intermediate complexity. It is an extension of the Zebiak and Cane (1987) model in that it is based on similar physics, that is, shallow water for both components. The ocean component includes three baroclinic modes, with characteristics of phase speed c_n , projection coefficient P_n , and “thermocline coefficient” scl_n (used to derive the thermocline fluctuations in a multimode context and depends directly on N^2 and the vertical derivative of the baroclinic mode vertical structures; see DEW for details) derived from Levitus et al. (1998). A mixed layer model is embedded in the ocean model that consists of a thermodynamic budget

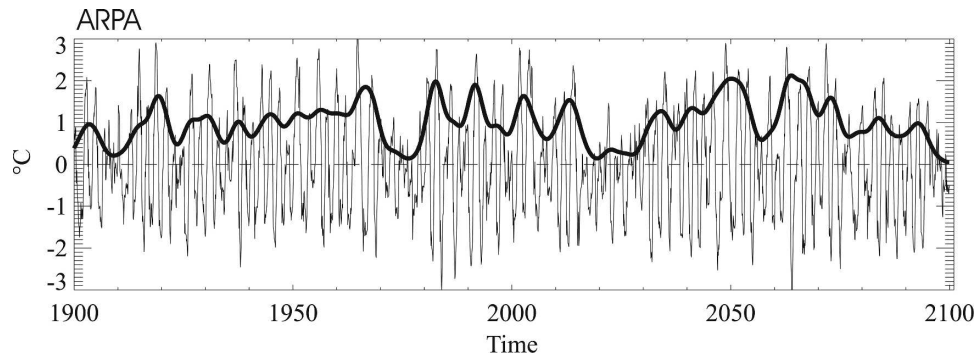


FIG. 3. (thin solid line) Niño-3 SST index of the CGCM simulation of Cibot et al. (2005) for the last 200 yr. The thick solid line stands for the N3VAR index as defined in Cibot et al. (2005), namely the integrated energy of the wavelet power spectrum of the Niño-3 SST index between 2- and 7-yr periods. Units are $^{\circ}\text{C}$ for the Niño-3 SST and N3VAR indices.

in a 50-m-thick surface layer. The surface heat flux is parameterized as being negatively proportional to local SST anomalies. Subsurface entrainment temperature into the surface mixed layer is parameterized as a function of thermocline depth anomalies and mean thermocline depth (Dewitte and Périgaud 1996). The reader is invited to refer to DEW for more details on this model.

LODCA was used to test the impact of parameter changes on simulated variability as described in section 4.

c. SODA

The SODA reanalysis project, which began in the mid-1990s, is an ongoing effort to reconstruct historical ocean climate variability on space and time scales similar to those acquired by the atmospheric reanalysis projects. The ocean model used for SODA is based on Geophysical Fluid Dynamics Laboratory Modular Ocean Model 2 (MOM2) physics (Pacanowski 1995) and has a resolution of $2.5^{\circ} \times 2.5^{\circ}$ in the Tropics, expanding to a uniform resolution of $2.5^{\circ} \times 1.5^{\circ}$ at middle latitudes (62°N and 62°S). The vertical mesh has a variable resolution with a maximum of 20 levels. The vertical resolution is 15 m at the surface, down to 150 m, with increasing resolution for the deepest level reaching 3600 m. The constraint algorithm is based on optimal interpolation data assimilation. Assimilated data include temperature and salinity profiles from the *World Ocean Atlas 1994* [mechanical bathythermograph (MBT), expendable bathythermograph (XBT), CTD, and station data], as well as additional hydrography, SST, and altimeter sea level. SODA data had average temperature and salinity errors in the upper 500 m of 0.70°C and 0.092 psu when compared with a series of global hydrographic sections. The reader is invited to

refer to Carton et al. (2000) for a detail description of the SODA system. For the research in this paper, the beta-6 version of the SODA dataset was used, consisting of monthly mean data between 1950 and 1998.

3. Decadal variability in ARPA

Following CMTD05, a 7-yr period threshold was chosen for the low-pass filter to be applied to the model outputs to investigate decadal variability in ARPA. Because the ENSO mode of the model is most energetic in the quasi-biennial band, the sensitivity of these results to the choice of the frequency cutoff for the filter is weak for frequencies ranging from 5 to 7 yr. In what follows we have thus concentrated on variability of the equatorial vertical structure without trying to relate it to the off-equatorial patterns that have been described in CMTD05. This has been attempted in the discussion section.

a. Temperature

As illustrated in CMTD05, the model produced an ENSO modulation that is a component of the decadal variability. Although there was a clear signature on the Niño-3 SST index (Fig. 3), this variability also projected on the upper 300 m of the whole water column and from west to east as illustrated by Fig. 4a, which shows the anomaly variability of the low-pass-filtered temperature as a function of depth. Two regions of large variability were identified above the thermocline: in the far-eastern Pacific (east of 120°W) and in the western Pacific near the date line. This is consistent with the observations of Luo and Yamagata (2001) and Moon et al. (2004). Interestingly, these two regions are separated by a zone of relative minimum variability near 60 m at 130°W , indicating that this pattern of variability is

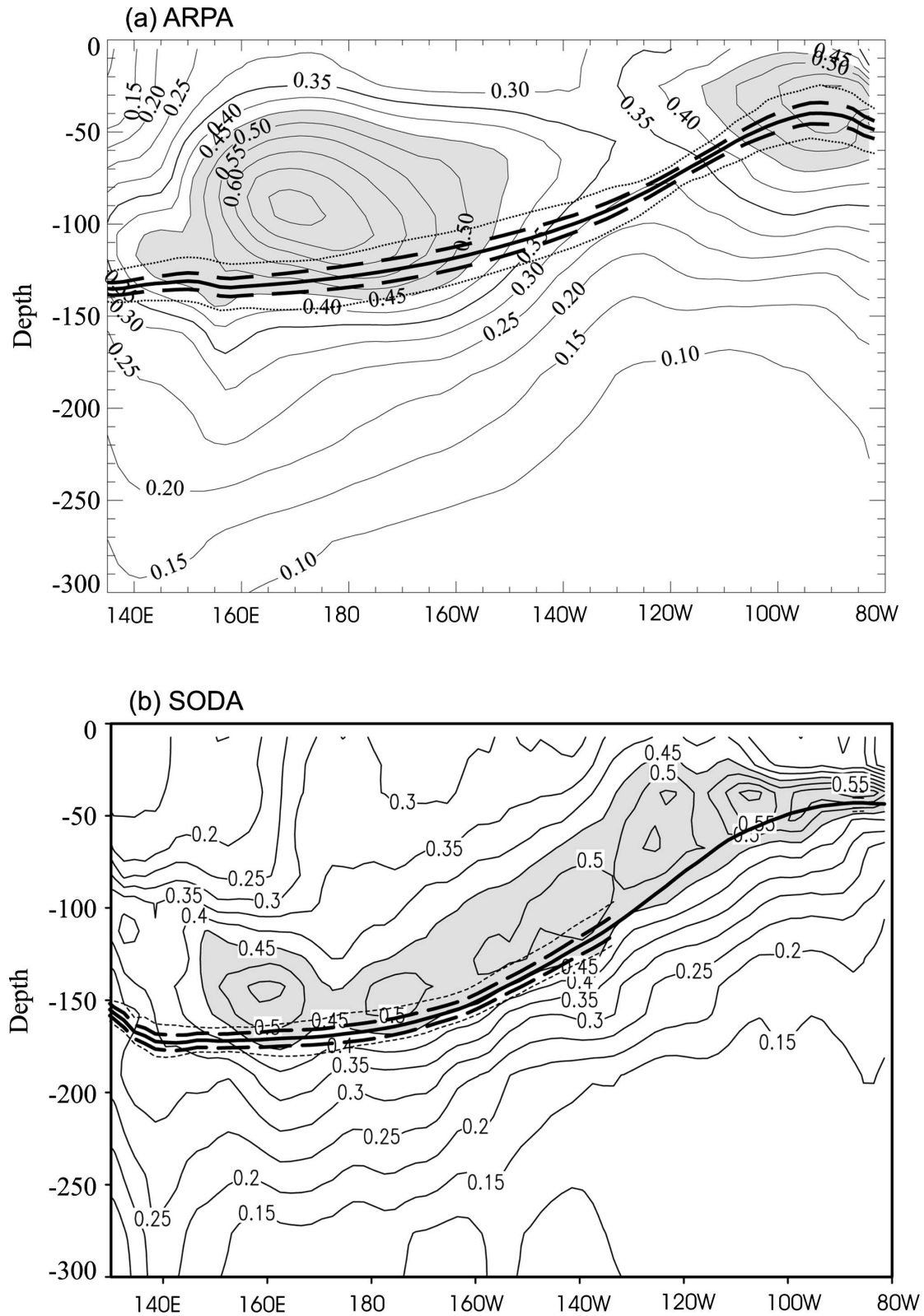


FIG. 4. The 7-yr low-pass-filtered temperature variability (rms) as a function of depth for (a) ARPA and (b) SODA data. The contour interval is 0.05°C . Shading is for values greater than 0.45°C . The mean thermocline depth (identified as the 20°C isotherm depth) is over plotted (thick solid line), along with rms deviation (dashed line) and maximum and minimum deviations of the 7-yr low-pass-filtered signal (thin dotted line).

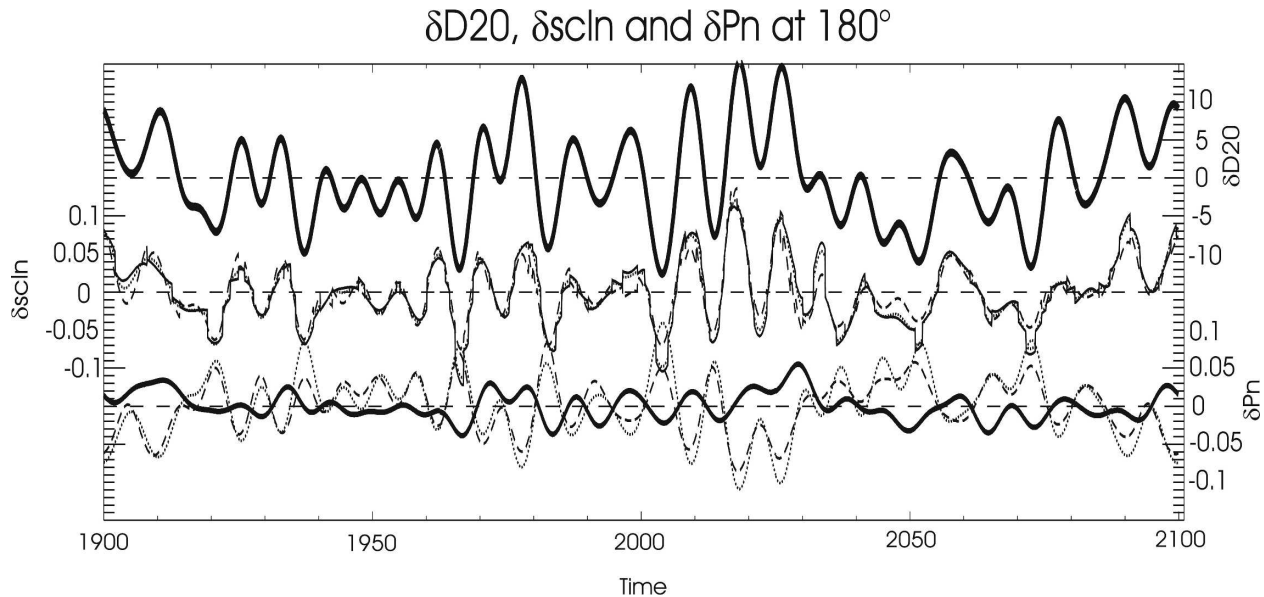


FIG. 5. (top) The 7-yr low-pass-filtered 20°C isotherm depth, (middle) variations in the “thermocline coefficient” δscl_n , induced by low-frequency variations in the 20°C isotherm depth and stratification, and (bottom) low-frequency component of the wind projection coefficient δP_n at (180°, equator) Units are meters for the 20°C isotherm depth anomalies; δscl_n is adimensionalized by $\{c_n^2/(g \times 150)\}$, where c_n is the phase speed of the considered baroclinic mode and g is the gravity acceleration; δP_n is adimensionalized using a multiplying factor of 150. The first (solid line), second (dotted line), and third (dashed line) baroclinic modes are displayed for δP_n and δscl_n .

related to the change in tilt of the mean thermocline slope. The pivot (zero crossing) of the decadal mode for the 20°C isotherm is indeed near 120°W (see Fig. 10 of CMTD05). Note that the peak in amplitude in the western Pacific is $\sim 30\%$ of the variability maximum of the 7-yr high-pass-filtered temperature anomaly in the same zone.

Another striking feature that emerged from an inspection of Fig. 4 was the relatively weak decadal variability of the 20°C isotherm depth (less than 10 m). Also, in the western Pacific, the peak zone of temperature variability was located ~ 50 m above the mean thermocline depth, which still above the shallowest thermocline position allowed by the 7-yr low-pass-filtered signal (upper thick dotted line). This is consistent with the fact that it has been difficult to characterize equatorial decadal variability through change in the mean thermocline depth from observations (Wang and An 2002). It thus appeared necessary to look at parameters that integrate the stratification changes in the vicinity of the thermocline and not just at the thermocline position. In comparison, the same figure is shown (Fig. 4b), but for the SODA outputs. Although covering a shorter period of time, SODA reveals comparable characteristics to the ones mentioned above with a maximum variability above the 20°C isotherm depth, which is itself subject to weak vertical displacements at the frequencies considered here. However, unlike

SODA, the maximum variability zones in ARPA do not spread continuously from west to east and the vertical scale of the variability maxima is somewhat larger.

b. Baroclinic mode fluctuations

The vertical modes were calculated in a similar way to the method used by Dewitte et al. (1999). The reader is invited to refer to this work for more technical details. To acquire the low-frequency changes in the mean stratification, the vertical mode decomposition was performed at each time step from the ARPA salinity and temperature averaged over the last 200 yr, on which the 7-yr low-pass-filtered signal was superimposed.

Such variations at decadal time scales of the mean equatorial vertical structure leave a signature on the baroclinic mode characteristics that can be quantified through the variations of the parameters (P_n, scl_n); P_n is the wind projection coefficient $P_n = [150/\int_{-H}^0 F_n^2(z) dz]$, and scl_n is the thermocline coefficient $scl_n = [g/N^2(z = \bar{h})] (dF_n/dz) (z = \bar{h})$, where $F_n(z)$ are the vertical mode structures and \bar{h} is the mean thermocline depth. These two parameters quantify the dynamic impact of stratification on the equatorial wave characteristics in a multibaroclinic mode context (see DEW for details).

Figure 5 shows the 7-yr low-pass-filtered 20°C isotherm depth anomalies (hereafter referred to as $\delta D20$)

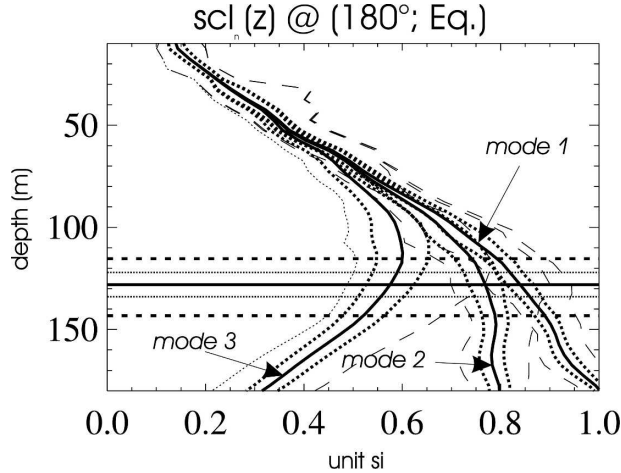


FIG. 6. Mean $scl_n(z)$ coefficient at 180° . Dashed profiles indicate maximum amplitude of positive and negative deviations of the decadal variability, whereas dotted profiles indicate the rms deviation of the 7-yr low-pass-filtered signal. The plain horizontal line indicates the mean thermocline depth at 180° and the horizontal dashed line indicate the maximum positive and negative deviations from this mean for the 7-yr low-pass-filtered signal. Rms deviation is also indicated (thin dotted line); scl_n has been adimensionalized by $\{c_n^2/(g \times 150)\}$, where c_n is the phase speed of the considered baroclinic mode and g is the gravity acceleration.

along with the deviations of the parameters P_n and scl_n (noted hereafter δP_n and δscl_n) from their mean values for the first three baroclinic modes. Here δscl_n was calculated with $z = \bar{h} + \delta D20$ and $F_n(z)$ evolving over time according to the slowly varying mean stratification, which can result in “jumps” resulting from the formulation (see equation above). Figure 6 illustrates the range of values that δscl_n can take as a function of depth and thermocline depth position. It is worth pointing out here that deriving δscl_n from the mean scl_n profiles [i.e., with constant $F_n(z)$], and for $z = \bar{h} + \delta D20$, leads to different behavior for this coefficient; in particular, for the third baroclinic mode, a deeper thermocline would result in a smaller scl_3 coefficient and consequently a negative value for δscl_3 (Fig. 5). For the same thermocline depth fluctuation, an opposite sign was obtained for δscl_3 when taking into account the actual change in the vertical structure function, that is, the temporally varying scl_n coefficient. Also, the magnitude of the δscl_n fluctuations was twice as large when considering the fluctuations in the vertical structure functions (not shown), which integrate changes in the stratification above the thermocline (and not only at the thermocline depth) as illustrated above. This illustrates that the relationship between δscl_n and $\delta D20$ is not linear.

From Fig. 5, it may first be noted that $\delta P_1(t)$ is anticorrelated with $\delta P_2(t)$ ($c = -0.60$) and $\delta P_3(t)$ ($c =$

-0.68), whereas δP_n reveals a high correlation for mode 1 and anticorrelation for modes 1 and 2 toward $\delta D20$. This indicates that a shallower (deeper) thermocline leads to a decreased (increased) contribution of the first baroclinic mode and an increased (decreased) contribution of the higher-order baroclinic modes. There is a different phase relationship between δscl_n and $\delta D20$ —a deeper (shallower) thermocline leads to larger (smaller) values of scl_n for the first three baroclinic modes. As mentioned above, this illustrates the subtle impact of the changes in stratification within the thermocline on the vertical mode structures, which could not be guessed from the sole variations of the mean thermocline depth and the average profiles of scl_n (cf. Fig. 6).

The maximum variations (in absolute value) of δP_n (δscl_n) reach 10% (14%), 20% (16%), and 36% (25%) of the mean for modes 1, 2, and 3, respectively, which is about 3 times more than for c_n (not shown). Note that a linear trend was retrieved, which was acquired by a former estimate of $P_1(t)$ performed during an early stage of this work. Interestingly, $\delta scl_1(t)$ and $\delta P_1(t)$ are uncorrelated ($c = 0.49$), whereas for modes 2 and 3, there is a high anticorrelation ($c = -0.89$ and $c = -0.87$). A closer inspection of Fig. 5 suggests that there is a time-lagged relationship between $\delta D20$ and δP_n and δscl_n as a function of the baroclinic mode order. Thus, $\delta D20$ leads δP_1 by 11 months ($c = 0.70$), whereas minimum correlation between $\delta D20$ and δP_2 and δP_3 is obtained at lag 0 ($c = -0.98$) and -2 ($c = -0.94$) months (δP_3 ahead), respectively. For δscl_n , the phase relationship with $\delta D20$ is at a maximum for lag +1 ($c = 0.87$), 0 ($c = 0.88$), and -2 ($c = 0.84$) months for modes 1, 2, and 3, respectively. This again illustrates the complex nature of the processes that may transmit the equatorial vertical structure variability to the ocean wave dynamics on decadal time scales.

Figure 7 illustrates the spatial pattern of the baroclinic mode energy distribution for the decadal to interdecadal variability in the form of maps of the surface current anomalies for the different baroclinic mode contributions. It should first be noted that the decadal variability is usually weaker by a factor of ~ 5 than the full interannual variability. Also, unlike the latter, the decadal variability of the surface currents is mostly concentrated in the western and central Pacific. More specific characteristics concern the meridional structure of the total surface current variability, which exhibits two regions of relative maximum at $5^\circ N$ and along the equator. This is also apparent for the first and second baroclinic mode contributions. Interestingly, the second and third modes peak up in the western Pacific, which is in some way a mirror picture of the results for the inter-

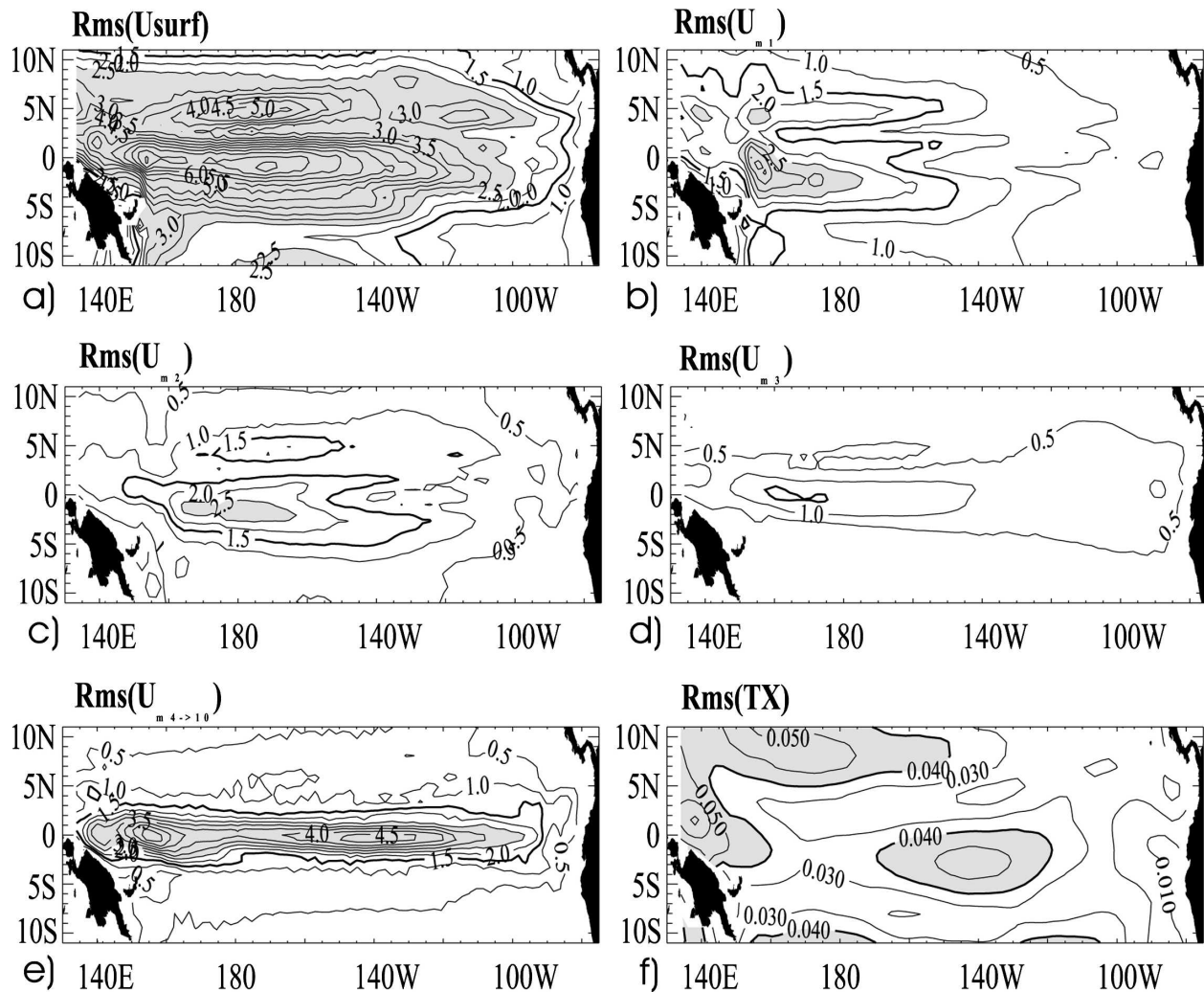


FIG. 7. Maps of variability (rms) of (a) the ARPA surface currents estimated as the average of the four top model levels; the contributions of the (b) first, (c) second, and (d) third baroclinic mode, and (e) sum of contributions of the fourth–tenth modes; and (f) of the zonal wind stress anomalies. Units are cm s^{-1} (Dyn cm^{-2}) and contour intervals are 0.5 cm s^{-1} (0.01 Dyn cm^{-2}) for currents (wind stress). Shading is for values above 2.5 cm s^{-1} (0.04 Dyn cm^{-2}) for currents (wind stress).

annual variability (not shown). The summed-up contribution of modes 4–10 has a central Pacific component, which is absent for the interannual variability and apparently related to local forcing. These results indicate that there is a different response of the coupled system according to the frequency domain (interannual versus interdecadal), and therefore that coupled processes specific to the interdecadal time scales can coexist with those that are associated with the interannual time scales (i.e., ENSO).

To check the consistency of the above results, similar calculations were performed using the SODA dataset. Figure 8 shows the low-frequency changes in the thermocline depth anomaly (20°C isothermal depth anomaly) and those of the wind projection coefficient

(P_n , $n = 1, 2, 3$) in the central equatorial Pacific (180°). The model $\delta\text{D}20$ and wind projection coefficient have relatively larger amplitudes than those in SODA. However, they have a comparable phase relationship. Note the impact of the climate shift around the late 1970s on P_1 , which corresponds to a decreasing thermocline depth. The relationship between $\delta\text{D}20$ and δP_n ($n = 1, 2, 3$) in the model shows some similarity compared to that of SODA. In particular, for SODA, it is clear that both δP_2 (-0.97) and δP_3 (-0.96) are anticorrelated to variations of $\delta\text{D}20$, suggesting that a shallower thermocline is associated with a larger contribution of the higher-order baroclinic modes. The relationship between δP_1 and δP_2 , δP_3 , and $\delta\text{D}20$ was not clear (i.e., no significant) for such a relatively short period of time.

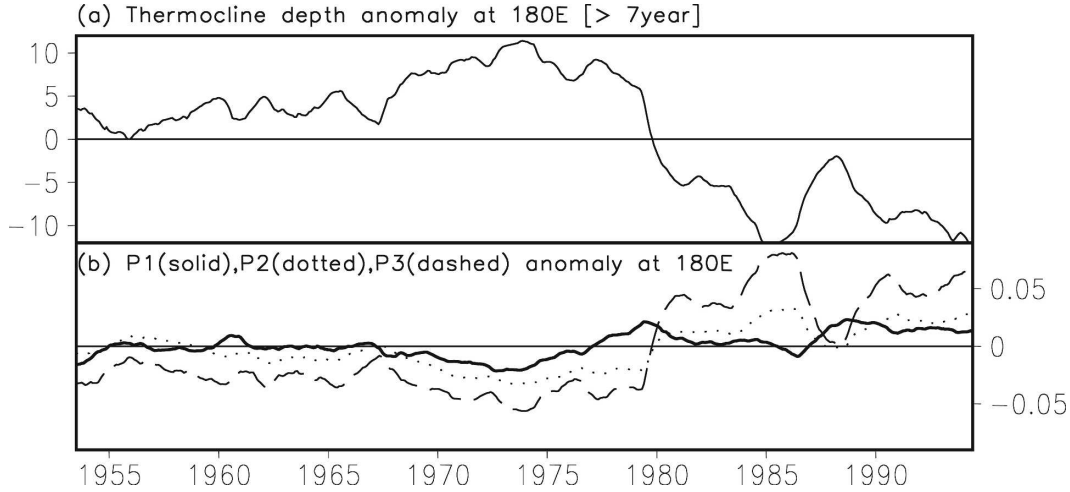


FIG. 8. The 7-yr low-pass-filtered (a) 20°C isotherm depth anomaly at 180°E and (b) the low-frequency component of the wind projection coefficient δP_n ($n = 1, 2, 3$) for the SODA data (1953–94). The first (solid), second (dotted), and third (dashed) baroclinic modes are displayed for δP_n . The unit is adimensionalized as for Fig. 5.

4. Intermediate coupled model experiments

This section describes the tests performed to determine whether the decadal signal of the wave parameters derived above could impact the interannual variability in an ICM to produce ENSO modulation. The ENSO modulation was quantified from an index, called N3VAR, which is defined as the integrated energy of the Niño-3-SST wavelet spectrum power in the 2–7-yr band (cf. CMTD05).

Figure 9 shows how neatly LODCA simulated the ARPA SST and its modulation in a forced mode, that is, when the ocean component of LODCA was forced with the ARPA monthly wind stress (heat flux forcing was not considered). Figure 9 can be directly compared to Fig. 3. Correlation values for the Niño-3 SST and N3VAR indices between ARPA and LODCA were above the 0.9 level, which indicated that the equatorial wave dynamics grasps most of the variability simulated by ARPA.

The approach therefore consisted of forcing the anomaly-coupled model with the interdecadal fluctuations of (P_n, scl_n) as derived from the CGCM simulation (“offline”), and then as derived from the simulated thermocline fluctuations of the ICM (“online”). These experiments made it possible first to determine whether or not any rectification took place, and second to investigate the rectified effect on the ENSO dynamics; third, they allowed for an analysis of the phase relationship between the ENSO modulation produced by the model and the prescribed (or parameterized) forcing.

a. Theoretical considerations: Uncoupled experiments

Let us first consider that a change at decadal time scales takes place through variations on the oceanic parameter. The variations in P_n and scl_n (i.e., δP_n and δscl_n) described above will lead to variations in the ocean dynamics (δu , δv , δw_s , δh) and therefore to SST changes in accordance with the following equation:

$$\begin{aligned} \frac{\partial T}{\partial t} = & -u(\bar{T} + T)_x - \bar{u}(T)_x - v(\bar{T} + T)_y - \bar{v}(T)_y - \gamma \\ & \times \{M(\bar{w}_s + w_s) - M(\bar{w}_s)\} \bar{T}_z - \gamma \\ & \times M(\bar{w}_s + w_s) \frac{T - T_{\text{sub}}(h, \bar{h})}{H_1} - \alpha T \end{aligned}$$

[$M(x)$ is a step function: $M(x) = x$ if $x \geq 0$; $M(x) = 0$ if $x < 0$].

Here T , (u, v, w_s) , and h stand for the anomalies for SST, the velocity field, and thermocline depth, respectively. Barred quantities represent climatological fields and unbarred quantities represent interannual anomalies relative to the seasonal cycle; α is a damping coefficient equal to $(115 \text{ days})^{-1}$.

The SST changes induced by $(\delta P_n, \delta scl_n)$, that is, $(\partial \delta T / \partial t)$, are controlled by a similar equation to the one above. It is then possible to assess which term of the SST equation is the most likely to amplify one feedback over the other (zonal advective feedback or thermocline feedback) by looking at the differences between the results of the forced LODCA runs with and

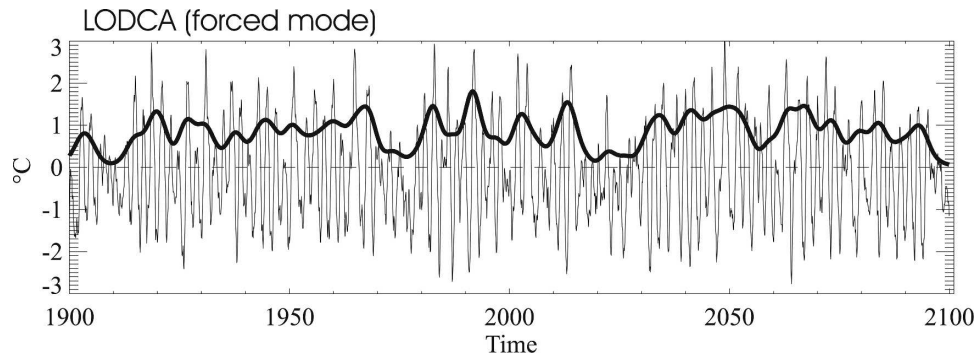


FIG. 9. Same as Fig. 3, but for LODCA forced by the ARPA wind stress anomalies.

without variations of (P_n, scl_n) . LODCA is then forced with the ARPA wind stress anomalies (uncoupled mode) with and without prescribed $(\delta P_n, \delta scl_n)$, and the difference between the two runs is analyzed. Figure 10a shows the root-mean-square and the skewness of this difference. For the sake of simplicity, and to ease the interpretation, the results for the meridional advection terms are not displayed. The variability (rms) of the difference in the atmospheric response (zonal wind stress anomaly) is also shown, indicating the location along the equator where air–sea interactions at an interdecadal time scale are likely to take place. It peaks in the central Pacific where air–sea interactions are the biggest at an interannual time scale, which indicates that $(\delta P_n, \delta scl_n)$ has the potential to affect the ENSO variability. Interestingly, the location of this peak coincides with the location of the maximum variability for the interdecadal component of the ARPA zonal wind stress anomalies (see Fig. 7f). The magnitudes of the variability peaks along the equator are also comparable (~ 0.04 versus ~ 0.02 Dyn cm^{-2}), considering the sensitivity of the result to the frequency cutoff of the low-pass filter applied to the ARPA outputs. Note that the amplitude of variability in wind stress induced by $(\delta P_n, \delta scl_n)$ is one order of magnitude less than the variability of the full zonal wind stress anomalies in the central Pacific. It is also worth pointing out that the spatial pattern of Fig. 7f differs from the variability maps of the interannual variability of zonal wind stress anomalies or of $\delta P_n(t)$. Here $\tau_x(t)$, with $\tau_x(t)$ standing for the zonal wind stress anomalies (not shown), which is consistent with the interpretation that the pattern of Fig. 7f, is indeed a signature of changes in the ocean dynamics rather than the imprint of δP_n on the flux momentum input.

The associated signature for SST (given by the term $-\alpha T$) peaks in the eastern Pacific and reaches $\sim 0.1^\circ\text{C}$. The skewness emphasizes regions where change in (P_n, scl_n) should favor either a warming or cooling, and

thereby the regions where nonlinear interactions are favored. Overall, the impact of $(\delta P_n, \delta scl_n)$ is a warming of the far-eastern Pacific and a cooling of the central Pacific. In the far-eastern Pacific, the zonal and vertical advection terms contribute with comparable amplitude. On the other hand, in the western Pacific, the variability for zonal advection is much larger than the vertical advection, which reflects the deeper thermocline and the contribution of high-frequency variability. Because temperature anomalies and zonal temperature gradients are small in that region, this does not have a direct impact on the atmospheric response. A check was made to ensure that the variability of the difference between the two runs for zonal advection was indeed associated with relatively high frequencies, with the variability for the 12-month high-pass-filtered data from the model outputs yielding comparable amplitude to that in Fig. 10a (not shown).

In the central Pacific, where the ocean–atmosphere coupling is the largest, the changes in mean stratification at decadal time scales tend to favor zonal advection over vertical advection. In particular, at 150°W the variability and skewness of anomalous advection of total temperature is twice as large as that of the other terms. This means that a change in mean state [associated with $(\delta P_n, \delta scl_n)$] will modify the stability of the coupled system. In particular, from the analytical work of Hirst (1986), the more intense zonal advection (through more intense surface currents) will favor greater destabilization of the advective Rossby-type instability of Hirst’s Model II. This Rossby-type mode is a fast westward-propagating mode (as opposed to the Kelvin-like instability of Hirst’s Model I), which suggests that wave dynamics associated with change in (P_n, scl_n) should favor a rather “fast” mode along the equator. This is consistent with the model simulating ENSO oscillations at periods of 2–3 yr rather than 3–5 yr, as observed.

To differentiate between the impact of δP_n and that of δscl_n , a LODCA simulation was performed in which

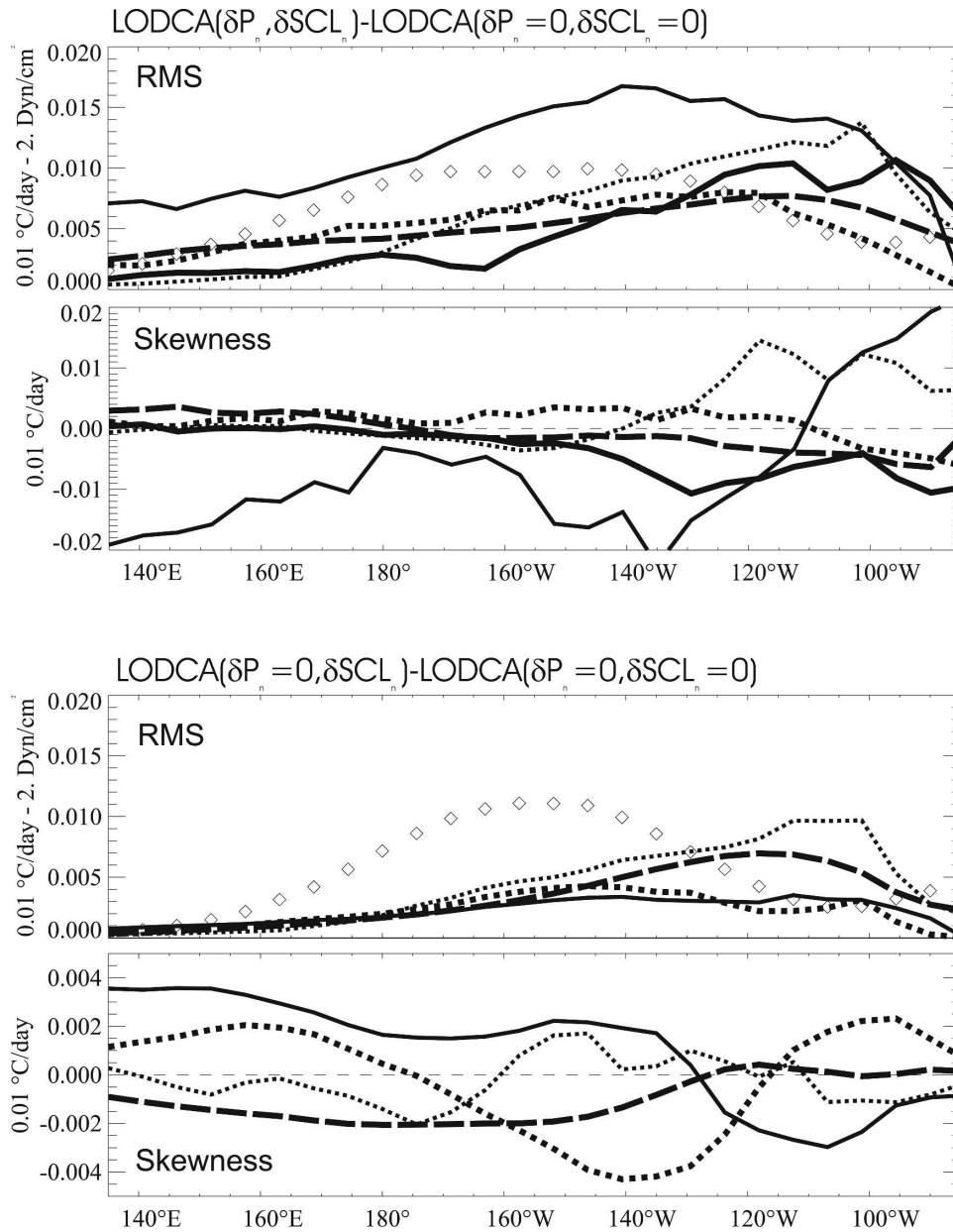


FIG. 10. (a) Root-mean-square and skewness of the difference between the LODCA runs forced by the ARPA wind stress anomalies with and without the variations in (P_n, scl_n) for the terms of the SST equations and the associated zonal wind stress anomalies along the equator: anomalous zonal current advection of total temperature (thin solid line), climatological zonal current of anomalous temperature (dotted line), anomalous vertical advection of mean temperature (thick solid line), climatological vertical advection of temperature anomaly (thick dotted line), damping term (thick dashed line), and zonal wind stress anomalies (diamonds). The units are $^\circ\text{C day}^{-1}$ for the SST equation terms (left-side axis) and Dyn cm^{-2} for wind stress (right-side axis). (b) Same as (a), but for the difference between the LODCA runs forced by the ARPA wind stress anomalies with and without the variations in scl_n only.

only a change in scl_n was prescribed. The difference with the LODCA reference run (i.e., with $\delta P_n = \delta scl_n = 0$) was analyzed in a similar way to that above (Fig. 10b). Note that δscl_n does not affect the anomalous vertical advection of mean temperature. Not surpris-

ingly, δscl_n affects the model variability less than δP_n because the energy distribution on the forced oceanic baroclinic modes was not changed. Mostly, δscl_n affects the mean vertical advection of anomalous temperature, causing positive skewness for SST (inverse of $-\alpha T$) in

the central and western Pacific where the asymmetry of the impact of thermocline depth fluctuations on SST (cooling effect versus warming effect) is the largest (Dewitte and Périgaud 1996). Note that the wind response variability is as large as for the experiment considering both the changes in (P_n, scl_n) mostly because of the stronger SST zonal gradients associated with δscl_n , which are only in the central equatorial Pacific. The effect of δscl_n is to warm the western and central equatorial Pacific and to produce easterlies, contributing destructively to the rectified effect of δP_n .

b. Coupled experiments

The above analysis and interpretation were then compared with the results of the LODCA runs, performed this time in a coupled mode, which enabled us to fully take into account the oceanic–atmospheric feedback associated with changes in the oceanic parameters and to test the hypothesis of the rectification of the interannual variability by changes in the mean stratification. The above ICM experiments were therefore repeated in a coupled mode to enable the changes in the ocean dynamics associated with $(\delta P_n, \delta scl_n)$ to feed back into the atmosphere. Two sets of experiments were then carried out, corresponding to different estimates of $(\delta P_n, \delta scl_n)$. In a first set of experiments, the $(\delta P_n, \delta scl_n)$ derived from ARPA were prescribed in LODCA for each time step. Thus, every 10 days (LODCA time step) changes in $(\delta P_n, \delta scl_n)$ induce changes in the wind stress forcing and thermocline depth fluctuations that lead to SST fluctuations capable of feeding back into the atmosphere. These can be considered as “pseudo” coupled experiments because prescribed “external” forcing is used for each time step. However, these experiments tested whether external decadal forcing could yield to ENSO modulations through changes in the mean parameters (P_n, scl_n) .

In order to test a “self-sustained” (i.e., without prescribed external forcing) equatorial mechanism for decadal variability associated with changes in (P_n, scl_n) , it is necessary to parameterize in the ICM, the way the low frequency changes in, say, thermocline depth fluctuation, feed back on $(\delta P_n, \delta scl_n)$. In other words, the simulated variability has to affect the mean state prescribed in the ICM. We propose here a simple parameterization based on the results of the previous section. Assuming that over a long enough period of time T the ICM simulates a mean change in thermocline depth fluctuation $\bar{\delta h} = (1/T) \int_t^{t+T} h dt$, it is then possible to relate this change to the changes in the (P_n, scl_n) parameters based on the ARPA analysis. In the light of the results of section 3 and to simplify matters, a linear

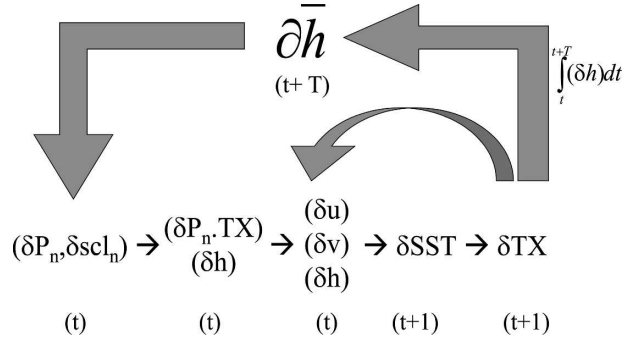


FIG. 11. Diagram showing the feedback processes associated with the slowly varying changes of (P_n, scl_n) .

fit was therefore performed between $\delta D20$, δP_n , and δscl_n , simulated in ARPA to derive a parameterization relating $\bar{\delta h}$ and $(\delta P_n, \delta scl_n)$ in LODCA, respectively. These feedback mechanisms are summarized in the diagram in Fig. 11.

1) COUPLED SIMULATIONS WITH PRESCRIBED $(\delta P_n, \delta scl_n)$

The Niño-3 SST and N3VAR indices for the LODCA simulation with and without prescribed $(\delta P_n, \delta scl_n)$ are shown in Figs. 12a,b. Consistent with results of section 4a, the results indicate that the impact of $(\delta P_n, \delta scl_n)$ on the model simulation is significant: Whereas the LODCA standard simulation does not reveal any ENSO modulation (Fig. 12a), the ENSO modulation (rms of N3VAR) in LODCA $(\delta P_n, \delta scl_n)$ reaches 26% of the variability of the Niño-3 SST index (Fig. 12b) (to be compared to 1% for Fig. 12a and 32% for Fig. 9).

To illustrate the effect of $(\delta P_n, \delta scl_n)$ on the simulated SST pattern, Fig. 13 shows the first EOF mode of the full and 7-yr low-pass-filtered SSTAs for the LODCA runs. Similar analyses for the ARPA SSTA (Figs. 13c,d) and for the LODCA reference run (Fig. 13e) are also shown for comparison. Interestingly, the decadal mode pattern for the LODCA simulation with $(\delta P_n, \delta scl_n)$ resembles that of ARPA with a zonal seesaw—warm in the east and cold in the west. The amplitude of the SST peaks is also comparable. Along with the fact that the LODCA reference run did not show a coherent decadal mode pattern (Fig. 13e), this suggests that part of the ARPA decadal SST variability is associated with changes in equatorial wave dynamics resulting from mean state fluctuations.

The experiments in which only one of the parameters $(P_n$ or $scl_n)$ was allowed to evolve over time (Figs. 13f,g) indicate that the changes in scl_n at decadal time scales apparently compensate for the changes associ-

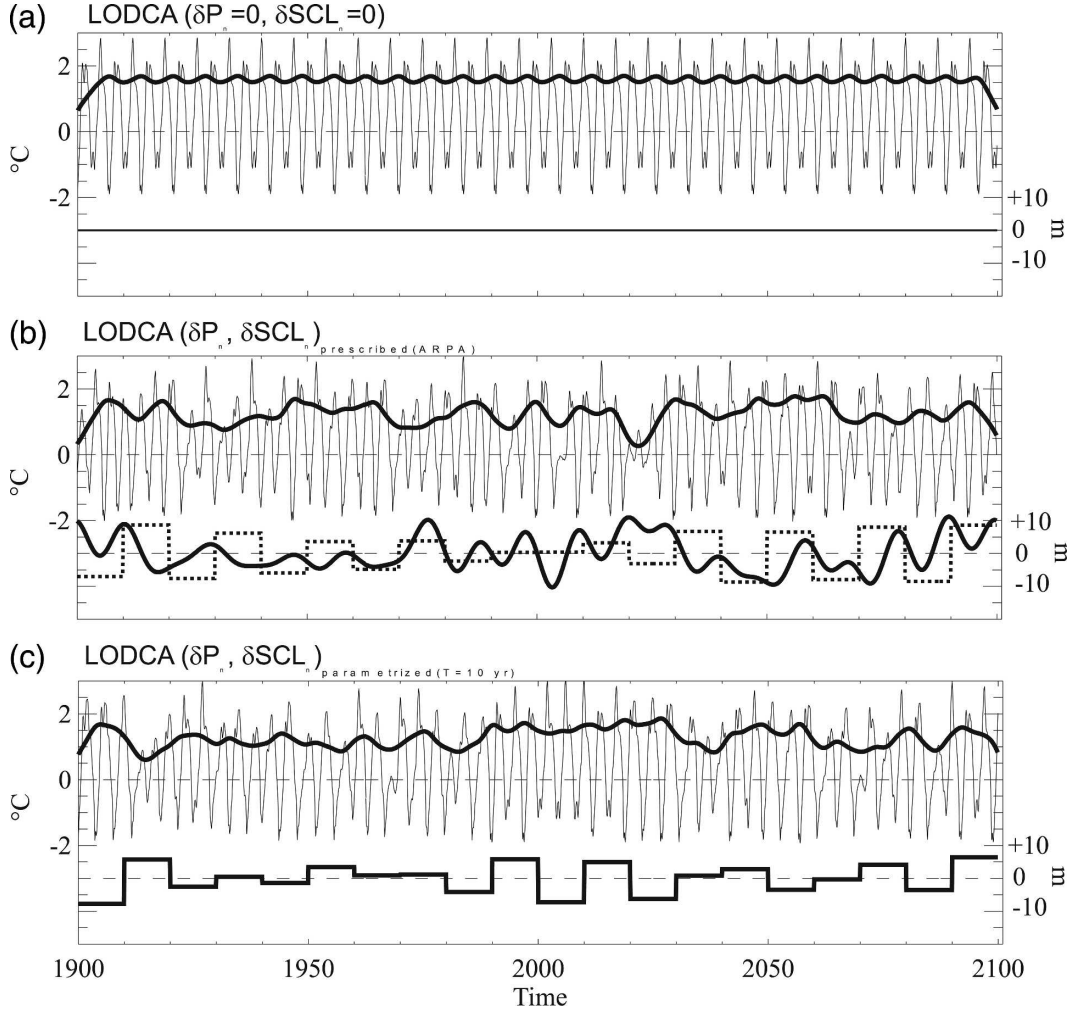


FIG. 12. Niño-3 SST and N3VAR indices for the LODCA coupled runs: (a) standard run without variation in (P_n, scl_n), (b) with ($\delta P_n, \delta scl_n$) as derived from ARPA, and (c) with parameterized ($\delta P_n, \delta scl_n$) taking $T = 10$ yr (see text). The corresponding variations in mean thermocline depth at 180° are plotted (plain thick line) below each Niño-3 SST series (scale on the right-hand side; units: m). For (b), the parameterized thermocline depth fluctuation is also plotted as a dotted line.

ated with P_n in LODCA and reduce the amplitude of the decadal mode in the eastern Pacific.

2) COUPLED SIMULATIONS WITH MODEL-DERIVED ($\delta P_n, \delta scl_n$)

We then test a rectification scenario according to which low-frequency changes in stratification are induced by nonlinearities associated with equatorial wave dynamics. As explained above (Fig. 11), the low-frequency fluctuations in the mean stratification were derived from the integration of the simulated thermocline anomalies at (180° , equator) over a period T (T ranging from 5 to 20 yr). The statistical relationship between $\delta D20$ and ($\delta P_n, \delta scl_n$) of ARPA were then

used to parameterize a feedback mechanism of the low-frequency ENSO variability. This relatively simple procedure enabled us to generate a set of simulations to test the robustness of the results derived earlier. Note that with the previous experimental settings [LODCA “forced” by ($\delta P_n, \delta scl_n$) as derived from ARPA], this parameterization led to a realistic amplitude/variability of the thermocline depth on low-frequency time scales at (180° , equator) (see dotted line in Fig. 12b). Results of the coupled experiment with LODCA, including this parameterization of low-frequency feedback ($T = 10$ yr), are shown in Fig. 12c for the Niño-3 SST index and associated N3VAR index. The model reveals an ENSO modulation that is comparable with the experiment with prescribed ($\delta P_n, \delta scl_n$) from ARPA ($\sim 25\%$ of the

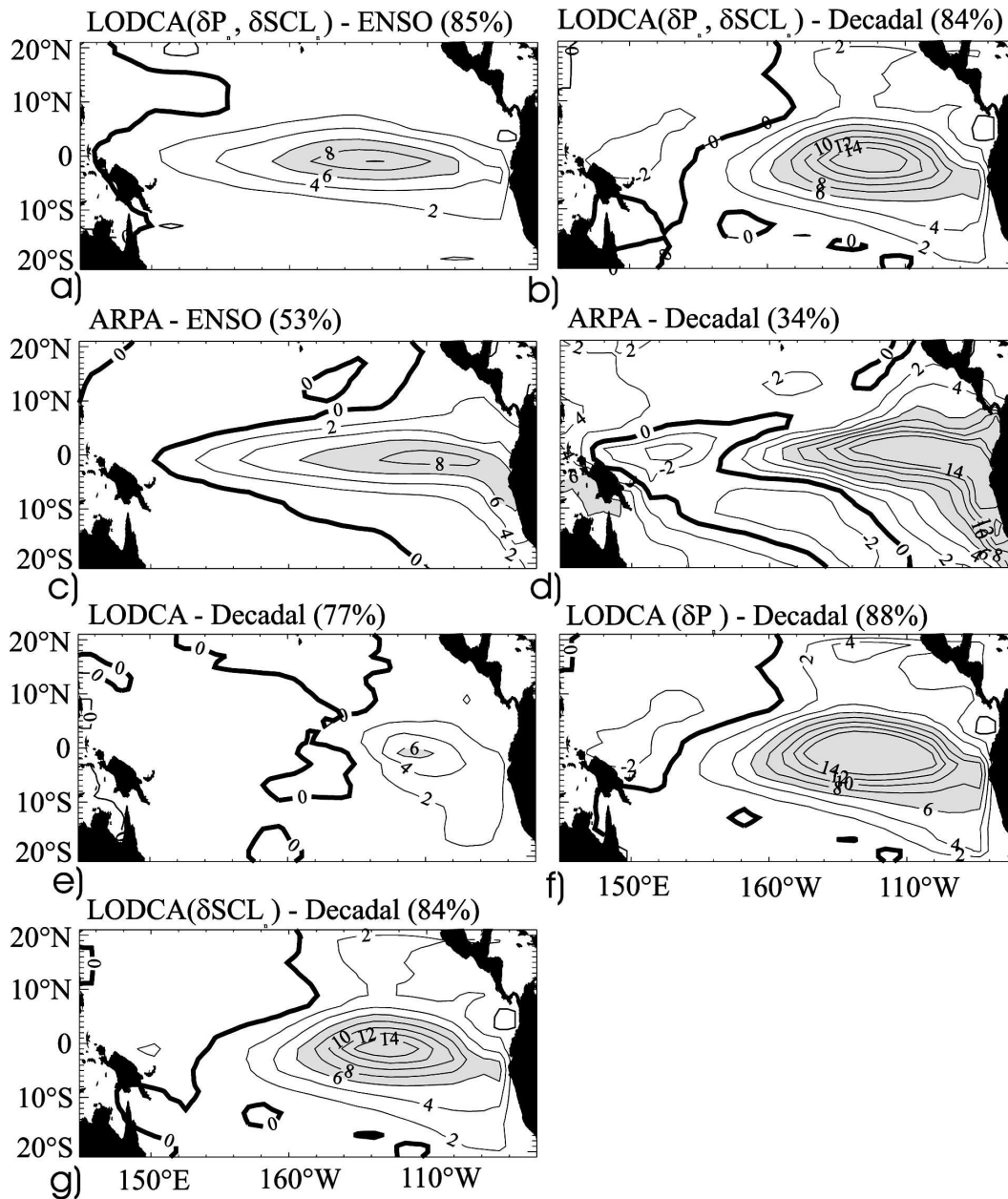


FIG. 13. Spatial pattern of the first EOF of the full (ENSO mode) and 7-yr low-pass-filtered (secadal mode) SSTA for the different coupled LODCA simulations and ARPA: (a), (b) LODCA with prescribed $(\delta P_n, \delta scl_n)$, (c), (d) ARPA, (e) LODCA with no $(\delta P_n, \delta scl_n)$, (f) LODCA with prescribed δP_n only, and (g) LODCA with prescribed δscl_n only. Units have been nondimensionalized. For all the simulations and ARPA, the variability of the associated time series is close to 0.2 and 0.02 for the full anomalies and the filtered anomalies, respectively, so that multiplying the spatial pattern by 0.2 and 0.02 provides an estimate of the values ($^{\circ}\text{C}$). The percentage of explained variance and the type of mode variability (ENSO or decadal) are indicated at the top of each map.

rms of the Niño-3 SST index). The dominant EOF of the 7-yr low-pass-filtered SSTAs are also comparable to the results in Fig. 13 (not shown).

Considering the nonlinearity associated with this mechanism, in particular concerning the asynchronicity of the feedback (the model “generating” its mean

change over a period T before it can affect the model variability), numerous experiments were performed with different values of T . Results are shown in Fig. 14 for the rms of N3VAR adimensionalized by the rms of Niño-3 SST. The low-frequency (i.e., at period T) thermocline depth variability has also been plotted. Inter-

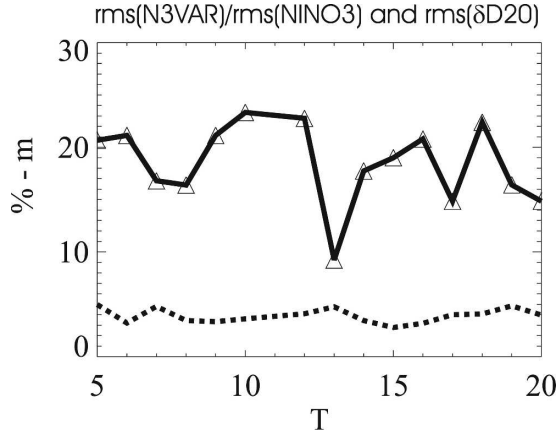


FIG. 14. Ratio of the rms of N3VAR to the rms of Niño-3 SST (%) (plain line), and low-frequency thermocline depth variability as a function of T (dotted line), the period over which thermocline depth anomalies are integrated to derive $(\delta P_n, \delta scl_n)$ for the experiments with LODCA (see text).

estingly, the rms of thermocline depth changes remains relatively weak (~ 5 m), comparable to ARPA and observations, for all the experiments. The magnitude of the ENSO modulation is also comparable for all the experiments.

3) PHASE RELATIONSHIP BETWEEN ENSO MODULATION AND CHANGES IN MEAN STATE

We then turned our attention to the question as to whether or not the ENSO modulation preceded or occurred after the change in mean state in the various ICM experiments. In a rectification process it is often difficult to answer this question, and in most coupled models a change in mean state and the ENSO modulation usually vary in phase (Rodgers et al. 2004; Luo et al. 2003; Yeh and Kirtman 2004). Figure 15 shows the time-lag correlation between the N3VAR index and the first PC time series for the 7-yr low-pass-filtered thermocline depth fluctuations for some of the experiments with LODCA and for ARPA. Consistent with the result of CMTD05 from yearly averaged model outputs, we find that in ARPA the ENSO modulation precedes the thermocline decadal mode (Z20DEC) by a few months (~ 5 months). The correlations higher than 0.4 are significant at the 95% confidence level. For the LODCA experiment with prescribed $(\delta P_n, \delta scl_n)$, the ENSO modulation is also ahead of Z20DEC, but with a reduced time lag. A variety of behavior is found for the LODCA experiments with parameterized $(\delta P_n, \delta scl_n)$ as a function of simulated thermocline anomalies. For a period T of less (larger) than ~ 8 yr, the simulated ENSO modulation tends to be behind (ahead) Z20DEC.

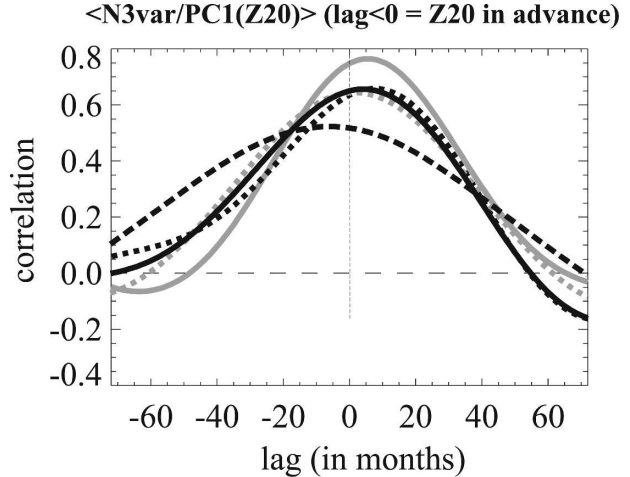


FIG. 15. Time-lag correlation between N3VAR and the first PC of the 7-yr low-pass-filtered thermocline depth for ARPA (plain gray line), the LODCA simulation with prescribed $(\delta P_n, \delta scl_n)$ from ARPA (dotted thick gray line), and three LODCA simulations with parameterized $(\delta P_n, \delta scl_n)$ with different values for T [$T=10$ yr (dotted black line), $T=15$ yr (plain black line), and $T=5$ yr (dashed black line)].

From these results, it was then not possible to conclude that ENSO modulation leads the thermocline depth on low-frequency time scales in the parameterized $(\delta P_n, \delta scl_n)$ experiment. It is noteworthy that the parameterized change in mean state of the various experiments carried out was never correlated to Z20DEC. This means that the model has a tendency to link changes in mean state (Z20DEC) and ENSO modulation (N3VAR), although the prescribed change in mean state is a highly nonlinear function of ENSO variability. This illustrates that Z20DEC is not a damped mode but results from a positive feedback between a change in mean state and ENSO modulation.

5. Discussion and conclusions

The low-frequency equatorial variability of a 260-yr full-physics CGCM simulation was investigated with a focus on the impact of low-frequency changes in the mean stratification on the ENSO modulations. Whereas the model exhibits a relatively weak thermocline depth change at decadal time scales as observed (Wang and An 2002), changes in mean temperature above the mean thermocline depth are significant. Concentrating on 7-yr low-pass-filtered CGCM outputs, these changes were quantified by estimating the shallow-water model parameters (P_n and scl_n) that partly control the relative strength of the thermocline and zonal advective feedbacks (cf. DEW). The results showed that the variations in the wind projection coef-

ficient P_n and the “thermocline coefficient” scl_n can reach up to 36% of their mean value for the first three baroclinic modes. A comparable magnitude of decadal changes in these parameters is obtained from the SODA oceanic reanalysis. Moreover, δP_1 is anticorrelated to $[\delta P_n(t)]_{(n=2,3)}$, which somehow overcomes the paradox explained in the introduction, according to which a flattening thermocline should be associated with reduced ENSO activity. A flattening thermocline is indeed related to a reduced P_1 that mimics the thermocline depth fluctuations. It is however also associated with an increased contribution of the high-order baroclinic modes (relevant to the stratification changes in the vicinity of the thermocline), which has the potential to burst the ENSO events through equatorial wave dynamics. Consistently with this interpretation, the high-order baroclinic mode contributions to zonal current anomalies revealed significant low-frequency variability with characteristics distinct from those associated with interannual anomalies. For instance, for mode 2, the maximum variability was located in the western Pacific for the decadal to interdecadal time scales, whereas it was located in the eastern Pacific for the interannual anomalies (Dewitte et al. 2007). The largest variability of the zonal current in the western Pacific at decadal time scales is consistent with the SST pattern of the decadal mode that reveals a zonal seesaw (with a pivot at the date line longitude), assuming that SST is mostly driven by zonal advection in the equatorial western Pacific. Note that, although not always as pronounced, a comparable zonal seesaw structure for the decadal SST mode is found in other recent modeling studies (Timmermann 1999, 2003; Rodgers et al. 2004; Yeh and Kirtman 2004).

We further tested in an ICM to determine whether the low-frequency changes in the mean stratification as diagnosed in this study had an effect on the simulated variability by producing ENSO modulations. Results of the experiments revealed that realistic ENSO modulation was generated when variations of (P_n, scl_n) , as derived from the CGCM simulation, were prescribed in the ICM. The rectified effect operated predominantly through the zonal advection terms, which tend to destabilize the coupled system toward a “faster” ENSO variability. The nonlinear zonal advection was also enhanced. Consistent with the theory developed by Timmermann (2003), this indicates that the nonlinearities associated with equatorial wave dynamics are capable of generating the decadal variability of ENSO. We suggest therefore that the change in baroclinic mode energy distribution associated with the change in mean stratification within the thermocline serves as a source

of the nonlinearities that contribute to ENSO modulation.

As a consequence of the rectified effect, we found that the ENSO modulation was highly correlated at time lags of less than 1 yr to the simulated low-frequency thermocline depth variability in all the experiments that were carried out with the ICM. Interestingly, the experiments with parameterized $(\delta P_n, \delta scl_n)$ led to no correlation between say δP_1 (which mimics the stratification changes as a consequence of the parameterization; see section 4b) and the simulated slowly varying thermocline depth. This suggested that the decadal mode of SST (or thermocline depth) was not a damped and stochastically forced mode, but that it results from a positive feedback between changes in mean state and the ENSO modulation. This leaves space for many possibilities for the triggering mechanism of this rectified effect. The trigger could be of either stochastic or extratropical origin. Note that in the nonlinear scenario, no triggering mechanism is needed.

In the CGCM simulation used in this study, the thermocline decadal mode has its maximum variability in the southwestern Pacific (near 8°S), which is forced through Ekman pumping by the atmospheric response to ENSO SST modulation (see CMTD05 for details). Along the equator at 180°, the variability of this decadal mode pattern corresponds to the low-frequency change in thermocline depth used to derive P_n and scl_n . Note that similar characteristics of the decadal mode of thermocline depth are found in the SODA dataset (not shown) and the modeling studies of Luo et al. (2003) and Rodgers et al. (2004). This suggests a possible tropical mechanism for the ENSO modulation in the model; that is, the changes in equatorial wave dynamics associated with low-frequency fluctuation of the equatorial mean thermocline produce the ENSO modulation that forces the basin-wide decadal mode of thermocline depth through Ekman pumping with a center of action in the southwestern Pacific (see Fig. 12 of CMTD05). This is consistent with ENSO nonlinearity, as measured by SSTA skewness, being related to changes in mean state in the tropical Pacific (Fig. 2).

We shall now point out limitations arising from the use of an anomaly ICM as a support for quantifying the rectified effect associated with a change in mean state. First, the magnitude of the ENSO modulation depends on the characteristics of the climatologies that are prescribed in the ICM. Dewitte et al. (2007) have shown that the interaction between the mean state and the ENSO mode can lead to a different behavior of the coupled system. In particular, depending on the characteristics of the prescribed climatological mean state, it can result in a different time scale of the variability

for the ENSO mode, ranging from 2.5 yr for LODCA, using a prescribed climatological state as derived from ARPA, to 4.5 yr in the case of LODCA configured as in DEW. Sensitivity experiments with the ICM suggest that the impact of decadal changes in the mean state is less (in terms of magnitude of the ENSO modulation) when the climatological mean states of ARPA are prescribed in LODCA. However in that case it is difficult to quantify the effect of $(\delta P_n, \delta scl_n)$ because the “free” model in that configuration has already revealed a significant ENSO modulation (not shown). This is partly due to the nonlinear interaction between an enhanced near-annual mode and the ENSO variability, with the near-annual mode acting as a “noise maker” for the ENSO mode in ARPA (see Dewitte et al. 2007 for details). In the absence of an overenergetic near-annual mode, more coherency between changes in the mean state and the ENSO modulation is expected because the changes in mean thermocline depth and associated $(\delta P_n, \delta scl_n)$ are more directly “forced” by the ENSO modulation. On the other hand, less energy may be provided to the system to enhance the feedback mechanism proposed here. This needs to be further investigated from CGCMs, which behave more realistically with regards to the time scale of ENSO and near-annual mode activity.

In this study, another concern is that we concentrated on the effect on low-frequency change in thermocline depth and associated stratification variability, whereas there are other parameters not directly related to thermocline depth that are also capable of affecting the ICM behavior. In particular, one could have prescribed changes in mean zonal currents or SSTs, which also directly affect the advection terms in the mixed layer. Whereas the mean SST revealed a relatively weak variation at a decadal time scale, the zonal current decadal variability was more significant than its mean value. In the central Pacific, where mean zonal currents are weak, the variability can reach $\sim 10 \text{ cm s}^{-1}$ (see Fig. 7a), which has the ability to influence the coupled system through the rectified effect associated with zonal advection of temperature. Note, however, that considering $(\delta P_n, \delta scl_n)$ in a forced simulation of LODCA, and comparing them to the LODCA outputs without $(\delta P_n, \delta scl_n)$ (same experiments as in section 4a), results in a pattern of variability for surface zonal current that resembles the low-frequency component of the ARPA zonal current (Fig. 7a). This suggested that low-frequency changes in the zonal current climatological state are a result of changes in the equatorial dynamics associated with a change in mean stratification rather than a cause of these changes. At that stage, it becomes difficult to disentangle the effect from the cause.

For simplicity, we have chosen not to consider such changes.

To sum up, we have proposed a mechanism for decadal variability in the tropical Pacific. Such a mechanism is consistent with the theory developed by Timmermann (2003), which attributes the main role in creating decadal variability to the nonlinearities of the system. The paradigm for producing ENSO modulation proposed here also implicitly includes the An and Jin (2000) interpretation of tropical decadal variability. Changes in the oceanic parameters (P_n, scl_n) indeed have the ability to favor or prejudice the zonal advective feedback versus the thermocline feedback through changes in baroclinic mode energy distribution, which in turn leads to low-frequency SST variability. The tropical atmospheric bridge that links the ENSO SST modulation to the thermocline depth variability in the southwestern Pacific, building the tropical thermocline depth on decadal time scales in the model (cf. CMTD05), is another component of this mechanism that deserves further study based on observations and other model outputs. In particular, there is a variety of behavior in CGCMs concerning the sources of mean thermocline variability in the south central and western tropical Pacific. Whether or not the latter is associated with local forcing and/or propagation of spiciness anomalies from the subduction regions of the southeastern Pacific remains an issue of debate in the community. Forced OGCM simulation suggests that density-compensating anomalies of temperature and salinity may propagate westward and equatorward from the southeastern Pacific (Yeager and Large 2004), but the role of surface forcing affecting these spiciness anomalies appears to be complex because the isopycnals are themselves influenced by the basin-wide forcing, water mass formation, and transformation and ocean dynamics. In the CGCM simulation used in this study, there was no propagation of spiciness anomalies up to the equatorial regions (CMTD05), which supports the hypothesis of a tropical basin-wide forced decadal mode. In addition, the noise-marker near-annual mode mentioned above (Dewitte et al. 2007) may also act as a source for the SST variability of the SST equation terms, which includes nonlinear dynamical heating (Timmermann 2003), and may provide the energy for this feedback mechanism to be sustained. This needs further investigation and clues for resolving this question may be found through an inspection of CGCM simulations that reveal different characteristics of both their mean state and ENSO nonlinearity, as is the case for the coupled model intercomparison project simulations (An et al. 2005).

Acknowledgments. The authors thank the two anonymous reviewers for their helpful comments and suggestions, and also Dr. Soon-Il An for fruitful discussions and for providing Fig. 1. The authors would also like to thank Yves du Penhoat who was instrumental in the initial stage of this work. Stimulating discussions with Dr. Geert Jan van Oldenborgh and Dr. Henk Dijkstra during the First Alexander von Humboldt International Conference in Ecuador (May 2005) were also greatly appreciated. S.-W. Yeh was supported by the Korea Meteorological Administration Research and Development Program under Grant CATER 2006-4202.

REFERENCES

- An, S.-I., 2004: Interdecadal changes in the El Niño–La Niña asymmetry. *Geophys. Res. Lett.*, **31**, L23210, doi:10.1029/2004GL021699.
- , and F.-F. Jin, 2000: An eigen analysis of the interdecadal changes in the structure and frequency of ENSO mode. *Geophys. Res. Lett.*, **27**, 2573–2576.
- , and —, 2004: Nonlinearity and asymmetry of ENSO. *J. Climate*, **17**, 2399–2412.
- , Y.-G. Ham, J.-S. Kug, F.-F. Jin, and I.-S. Kang, 2005: El Niño–La Niña asymmetry in the coupled model intercomparison project simulations. *J. Climate*, **18**, 2617–2627.
- Barnett, T. P., D. W. Pierce, M. Latif, D. Dommenges, and R. Saravanan, 1999: Interdecadal interactions between the tropics and midlatitudes in the Pacific basin. *Geophys. Res. Lett.*, **26**, 615–618.
- Carton, J. A., G. Chepurin, X. Cao, and B. Giese, 2000: A simple ocean data assimilation analysis of the global upper ocean 1950–95. Part I: Methodology. *J. Phys. Oceanogr.*, **30**, 294–309.
- Cibot, C., E. Maisonnave, L. Terray, and B. Dewitte, 2005: Mechanisms of tropical Pacific interannual-to-decadal variability in the ARPEGE/ORCA global coupled model. *Climate Dyn.*, **24**, 823–842.
- Déqué, M., C. Dreveton, A. Braun, and D. Cariolle, 1994: The climate version of ARPEGE/IFS: A contribution to the French community climate modeling. *Climate Dyn.*, **10**, 249–266.
- Dewitte, B., 2000: Sensitivity of an intermediate ocean–atmosphere coupled model of the tropical Pacific to its oceanic vertical structure. *J. Climate*, **13**, 2363–2388.
- , and C. Pérégaud, 1996: El Niño–La Niña events simulated with Cane and Zebiak’s model and observed with satellite or in situ data. Part II: Model forced with observations. *J. Climate*, **9**, 1188–1207.
- , G. Reverdin, and C. Maes, 1999: Vertical structure of an OGCM simulation of the equatorial Pacific Ocean in 1985–94. *J. Phys. Oceanogr.*, **29**, 1542–1570.
- , C. Cibot, C. Pérégaud, S.-I. An, and L. Terray, 2007: Interaction between near-annual and ENSO modes in a CGCM simulation: Role of the equatorial background mean state. *J. Climate*, **20**, 1035–1052.
- Fichefet, T., and M. A. Morales Maqueda, 1997: Sensitivity of a global sea ice model to the treatment of ice thermodynamics and dynamics. *J. Geophys. Res.*, **102**, 12 609–12 646.
- Gu, D., and S. G. H. Philander, 1995: Secular changes of annual and interannual variability in the Tropics during the past century. *J. Climate*, **8**, 864–876.
- , and —, 1997: Interdecadal climate fluctuations that depend on exchanges between the tropics and extratropics. *Science*, **275**, 805–807.
- Guillemont, T. P., and D. P. Schrag, 1998: Abrupt shift in subsurface temperatures in the tropical Pacific associated changes in El Niño. *Science*, **281**, 240–243.
- Hirst, A. C., 1986: Unstable and damped equatorial modes in simple coupled ocean–atmosphere models. *J. Atmos. Sci.*, **43**, 606–632.
- Kirtman, B. P., and P. S. Schopf, 1998: Decadal variability in ENSO predictability and prediction. *J. Climate*, **11**, 2804–2822.
- Kleeman, R., Jr., and B. A. Klinger, 1999: A mechanism for generating ENSO decadal variability. *Geophys. Res. Lett.*, **26**, 1743–1746.
- Knutson, T. R., S. Manabe, and D. Gu, 1997: Simulated ENSO in a global coupled ocean–atmosphere model: Multidecadal amplitude modulation and CO₂ sensitivity. *J. Climate*, **10**, 138–161.
- Latif, M., and T. P. Barnett, 1994: Causes of decadal climate variability over the North Pacific and North America. *Science*, **266**, 634–637.
- , and —, 1996: Decadal climate variability over the North Pacific and North America: Dynamics and predictability. *J. Climate*, **9**, 2407–2423.
- Levitus, S., and Coauthors, 1998: *Introduction*. Vol. 1, *World Ocean Database 1998*, NOAA Atlas NESDIS 18, 346 pp.
- Luo, J.-J., and T. Yamagata, 2001: Long-term El Niño–Southern Oscillation (ENSO)-like variation with special emphasis on the South Pacific. *J. Geophys. Res.*, **106**, 22 211–22 228.
- , S. Masson, S. Behera, P. Delecluse, S. Gualdi, A. Navarra, and T. Yamagata, 2003: South Pacific origin of the decadal ENSO-like variation as simulated by a coupled GCM. *Geophys. Res. Lett.*, **30**, 2250, doi:10.1029/2003GL018649.
- Mantua, N. J., and S. R. Hare, 2002: The Pacific decadal oscillation. *J. Oceanogr.*, **58**, 35–44.
- McCreary, J., Jr., and P. Lu, 1994: Interaction between the subtropical and equatorial ocean circulations: The subtropical cell. *J. Phys. Oceanogr.*, **24**, 466–497.
- Miller, A. J., D. R. Cayan, T. P. Barnett, N. E. Graham, and J. M. Oberhuber, 1994a: The 1976–77 climate shift of the Pacific Ocean. *Oceanography*, **7**, 21–26.
- , —, —, —, and —, 1994b: Interdecadal variability of the Pacific Ocean: Model response to observed heat flux and wind stress anomalies. *Climate Dyn.*, **9**, 287–302.
- Moon, B.-K., S.-W. Yeh, B. Dewitte, J.-G. Jhun, I.-S. Kang, and B. Kirtman, 2004: Vertical structure variability in the equatorial Pacific before and after the Pacific climate shift of the 1970s. *Geophys. Res. Lett.*, **31**, L03203, doi:10.1029/2003GL018829.
- Pacanowski, R. C., 1995: MOM 2 documentation user’s guide and reference manual, version 1.0. GFDL Tech. Rep. 3, 232 pp.
- Rasmusson, E. M., and T. H. Carpenter, 1982: Variations in tropical sea surface temperature and surface wind fields associated with the Southern Oscillation/El Niño. *Mon. Wea. Rev.*, **110**, 354–384.
- Rodgers, K. B., P. Friederichs, and M. Latif, 2004: Tropical Pacific decadal variability and its relation to decadal modulations of ENSO. *J. Climate*, **17**, 3761–3774.
- Roulet, G., and G. Madec, 2000: Salt conservation, free surface, and varying volume: A new formulation for ocean general circulation models. *J. Geophys. Res.*, **105**, 23 927–23 942.

- Smith, T. M., and R. W. Reynolds, 2004: Improved extended reconstruction of SST (1854–1997). *J. Climate*, **17**, 2466–2477.
- Terray, L., E. Sevault, E. Guilyardi, and O. Thual, 1995: OASIS 2.0: User's guide and reference manual. CERFACS Tech. Rep. TR/CMGC/95-46, 123 pp.
- Timmermann, A., 1999: Detecting the nonstationary response of ENSO to greenhouse warming. *J. Atmos. Sci.*, **56**, 2313–2325.
- , 2001: Changes of ENSO stability due to greenhouse warming. *Geophys. Res. Lett.*, **28**, 2061–2064.
- , 2003: Decadal ENSO amplitude modulations: A nonlinear paradigm. *Global Planet. Change*, **37**, 135–156.
- , and F. F. Jin, 2002: A nonlinear mechanism for decadal El Niño amplitude changes. *Geophys. Res. Lett.*, **29**, 1003, doi:10.1029/2001GL013369.
- , M. Latif, A. Bacher, J. Oberhuber, and E. Roeckner, 1999: Increased El Niño frequency in a climate model forced by future greenhouse warming. *Nature*, **398**, 694–696.
- , F.-F. Jin, and J. Abshagen, 2003: A nonlinear theory for El Niño bursting. *J. Atmos. Sci.*, **60**, 152–165.
- Torrence, C., and P. J. Webster, 1999: Interdecadal changes in the ENSO–monsoon system. *J. Climate*, **12**, 2679–2690.
- Tourre, Y. M., Y. Kushnir, and W. B. White, 1999: Evolution of interdecadal variability in sea level pressure, sea surface temperature, and upper ocean temperature over the Pacific Ocean. *J. Phys. Oceanogr.*, **29**, 1528–1541.
- , C. Cibot, L. Terray, W. B. White, and B. Dewitte, 2005: Quasi-decadal and inter-decadal climate fluctuations in the Pacific Ocean from a CGCM. *Geophys. Res. Lett.*, **32**, L07710, doi:10.1029/2004GL022087.
- Trenberth, K. E., 1997: The definition of El Niño. *Bull. Amer. Meteor. Soc.*, **78**, 2771–2777.
- , and J. W. Hurrell, 1994: Decadal atmosphere–ocean variations in the Pacific. *Climate Dyn.*, **9**, 303–319.
- Urban, F. E., J. E. Cole, and J. T. Overpeck, 2000: Modification of tropical Pacific variability by its mean state inferred from a 155-year coral record. *Nature*, **407**, 989–993.
- Vimont, D. J., D. S. Battisti, and A. C. Hirst, 2002: Pacific interannual and interdecadal equatorial variability in a 1000-yr simulation of the CSIRO coupled general circulation model. *J. Climate*, **15**, 160–178.
- Wang, B., 1995: Interdecadal changes in El Niño onset in the last four decades. *J. Climate*, **8**, 267–285.
- , and S.-I. An, 2002: A mechanism for decadal changes of ENSO behavior: Roles of background wind changes. *Climate Dyn.*, **18**, 475–486.
- Yeager, S. G., and W. G. Large, 2004: Late-winter generation of spiciness on subducted isopycnals. *J. Phys. Oceanogr.*, **34**, 1528–1547.
- Yeh, S.-W., and B. P. Kirtman, 2004: Tropical Pacific decadal variability and ENSO amplitude modulation in a CGCM. *J. Geophys. Res.*, **109**, C11009, doi:10.1029/2004JC002442.
- , B. Dewitte, J.-G. Jhun, and I.-S. Kang, 2001: The characteristic oscillation induced by coupled processes between oceanic vertical modes and atmospheric modes in the tropical Pacific. *Geophys. Res. Lett.*, **28**, 2847–2850.
- Zebiak, S. E., and M. A. Cane, 1987: A model El Niño–Southern Oscillation. *Mon. Wea. Rev.*, **115**, 2262–2278.
- Zhang, Y., J. M. Wallace, and D. S. Battisti, 1997: ENSO-like interdecadal variability: 1900–93. *J. Climate*, **10**, 1004–1020.